AIAA Aviation Forum 2023, San Diego, California

Multi-Fidelity Computational Analysis of a Quiet Single-Main Rotor Helicopter for Air Taxi Operations

Patricia Ventura Diaz*, David Garcia Perez†, and Seokkwan Yoon‡
NASA Ames Research Center, Moffett Field, California, 94035

A multi-fidelity computational study has been conducted on NASA's quiet single-main rotor helicopter concept for urban air mobility using computational fluid dynamics and rotorcraft comprehensive analysis tools. Two approaches have been followed in order to simulate the rotor flows: (1) a rotor disk model, which models the rotors as source terms, and (2) a high-fidelity approach using high-order accurate schemes and dual-time stepping, which simulates the rotor with its individual rotating blade grids. The delayed detached-eddy simulation model has been employed. A loose-coupling approach between the flow solver and a rotorcraft comprehensive code is utilized to include vehicle trim and motion variables. The quiet single-main rotor helicopter is one of the conceptual designs intended to focus and guide NASA's research activities in support of aircraft development for vertical take-off and landing air taxi operations.

Nomenclature

Greek symbols

Symbol	Description
β_0	Coning angle
β_{1c}	Longitudinal flapping angle
β_{1s}	Lateral flapping angle
δ	Boundary layer thickness
ΔS	Grid spacing
Ω	Rotor rotational speed
ψ	Azimuth position
ρ	Fluid density
σ	Thrust-weighted solidity
θ_0	Collective angle
θ_{tw}	Linear twist

Roman symbols

Symbol	Description
a	Fluid speed of sound
c	Local rotor blade chord length
C'	Sectional blade chord force
d	Turbulent length scale
h	Flight altitude
M	Mach number
M'	Sectional blade pitching moment
M^2c_c	Sectional chord force coefficient
M^2c_m	Sectional pitching moment coefficient
M^2c_n	Sectional normal coefficient
N'	Sectional blade normal force
P	Rotor power
R	Rotor radius
r	Radial position
Re	Reynolds number
T	Rotor thrust
T_∞	Freestream temperature
V	Velocity
y^+	Non-dimensional viscous wall spacing

Subscripts

Subscript	Description
∞	Freestream
root	Blade root
tip	Blade tip
wake	Rotor wake

*Research Scientist, Science & Technology Corporation, Computational Physics Branch, Member AAIA.
†Research Scientist, Science & Technology Corporation, Computational Physics Branch, Member AIAA.
‡Chief, Computational Physics Branch.

I. Introduction

Urban Air Mobility (UAM) is envisioned to be an alternative way of air transportation in the urban areas, where air taxis and delivery drones will operate safely. The UAM industry is evolving rapidly and manufacturers are developing a wide variety of vehicle architectures to accommodate different mission profiles. Indeed, unconventional designs have multiplied in an attempt to leverage new propulsion technologies. Conventional aircraft represent only a small portion of the spectrum. This poses a new challenge for certification, which now becomes a more complex and uncertain process.

NASA's Revolutionary Vertical Lift Technology (RVLT) project is contributing to UAM by designing a set of conceptual vehicles, with the objective to focus and guide the research activities in support of emerging aviation markets [1]. The configurations include relevant technologies and features, and are intentionally generic, to differentiate them from industry vehicles [2]. The concept vehicles include quadrotor, side-by-side, lift+cruise, quiet single-main rotor, and tiltwing aircraft configurations.

While most of the vehicle designs considered for UAM have multiple rotors, an often disregarded configuration is the single-main rotor helicopter, despite its importance for its known path for certification. In this paper, the quiet single-main rotor (QSMR) helicopter concept based on the work by Johnson [3] will be analyzed by using high- and mid-fidelity Computational Fluid Dynamics (CFD). The QSMR vehicle, shown in Figure 1, consists of a single-main rotor helicopter with a NOTAR (NO TAil Rotor) anti-torque system instead of a tail rotor to reduce tail-rotor noise. It has been specifically designed for low-noise operations.

Fig. 1 Rendering of the quiet single-main rotor helicopter design for UAM.

Previous high-fidelity CFD work performed by the authors includes high-fidelity simulations of NASA's QSMR helicopter air taxi [4], NASA's tilt-wing [5], NASA's quadrotor [6], NASA's side-by-side air taxi concept [7], and small multi-rotor vehicles [8]. This work demonstrated that high-fidelity methods are the right tool to analyze the vehicle performance while capturing the relevant flow features and aerodynamic interactions. However, their resource-intense use renders them impractical in the preliminary stages of design, where the final geometry may not be established yet.

Other levels of approximation can be considered that put less demands on computational resources at the expense of sacrificing accuracy. For example, actuator disk models have been extensively used to study the rotor influence and reproduce rotor installation effects [9]. In its classical formulation, this model treats the rotor as an infinitely thin, permeable disk that sustains a steady pressure jump. Higher-level approximations allow to retain an unsteady framework while the computational cost is relaxed on the grid generation side. Our implementation of the model assumes a time-averaged effect of the rotor flow, and it is based on the previous work by Chaffin and Berry [10]. In order to improve the accuracy of the predictions, the CFD solver has been loosely coupled with a comprehensive code allowing for aerodynamics and trim state to be exchanged, as described by Ahmad [11]. The turnaround time is significantly reduced compared to blade-resolved cases and the results are promising, with the key features of the flow being captured [12].

The objective of the present work is to perform a multi-fidelity computational analysis of the QSMR vehicle for air taxi operations. The steady-state mid-fidelity rotor disk model simulations will be compared to the unsteady high-fidelity rotor simulations, where the rotor blades are simulated using dual-time stepping and overset curvilinear moving grids. Both the rotor disk and the blade-resolved CFD simulations are carried out with high-order accurate schemes and a hybrid turbulence model. In addition, the CFD solver is loosely coupled with a rotorcraft comprehensive code for rotor trim and motion variables.

II. Numerical Approach

The flow solver used in this study is NASA's OVERFLOW [13] CFD solver. OVERFLOW is a finite-difference, structured overset grid, high-order accurate Navier-Stokes flow solver. NASA's Chimera Grid Tools (CGT) [14] overset grid generation software is used for generating the overset grids of rotors and complete vehicles. Body-fitted curvilinear near-body (NB) grids are generated using CGT. The computational domain is completed with the generation of Cartesian off-body (OB) grids that are automatically generated prior to grid assembly using the domain connectivity framework in OVERFLOW-D mode. The current time-accurate approach consists of an inertial coordinate system where NB curvilinear O-grids for the rotor blades rotate through the fixed OB Cartesian grid system. OVERFLOW is loosely coupled with the helicopter comprehensive code CAMRAD II [15]. The CFD provides mid- or high-fidelity nonlinear aerodynamics that corrects the lifting line aerodynamic analysis from CAMRAD II. The comprehensive code performs the structural dynamics and trim calculations and gives the information to OVERFLOW. The loose coupling approach is modular and non-intrusive as the codes communicate through their respective input/output files.

The numerical approach and the coupling process are described in more detail in the following paragraphs.

A. Overset Grid Generation

The overset grid generation process using CGT may be decomposed into four steps: geometry processing, surface grid generation, volume grid generation, and domain connectivity [14].

The geometry is usually obtained from a computer-aided design (CAD) model or a 3D-scanning point cloud. In solid modeling, the boundary representation (BRep) of an object describes its boundaries holding both the topological entities and the geometric components [16]. A pre-processing step generates discrete surface representations from the analytical BRep solid contained in STEP or IGES files. Access to the model topology and entities is accomplished through EGADS (the Engineering Geometry Aircraft Design System) API, which is a foundational component of the Engineering Sketch Pad [16]. For each body in the geometry, the `egads2srf` tool generates a surface grid file containing a set of structured surface patches on tessellated untrimmed BRep faces. The CAD model for the QSMR fuselage is shown in Figure 2a. Figure 2b shows the structured untrimmed patches obtained using EGADS. A curve grid file is also created that contains structured curves on tessellated BRep edges. Both files are used as inputs in the overset surface grid generation step.

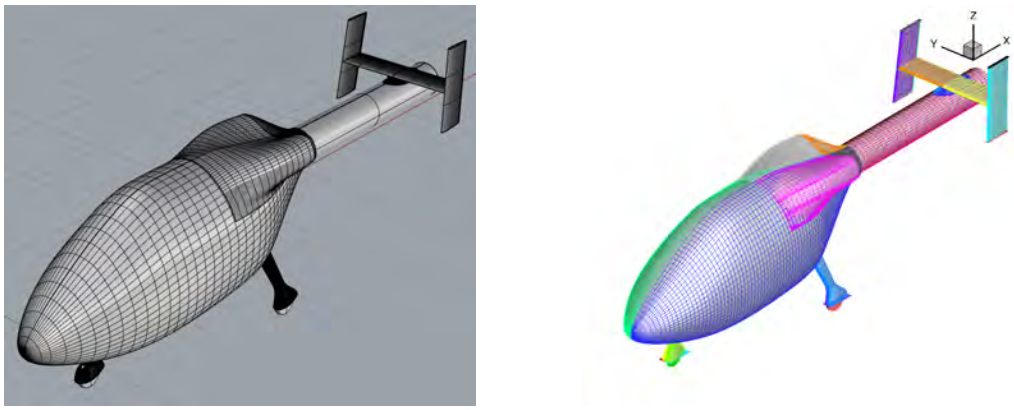

(a) CAD geometry. **(b) EGADS surface grid.**

Fig. 2 The quiet single-main rotor fuselage. Figure 2a shows the CAD geometry. Figure 2b shows the structured untrimmed patches obtained from the CAD geometry using EGADS. The patches are used as reference surfaces to generate the overset surface grids.

Once the geometry has been processed as reference curve and surface files, structured surface grids are generated using a combination of algebraic and hyperbolic methods. The generation of surface grids is the step that requires the most manual effort and experience from the user. Figure 3 shows the overset surface grids for the two configurations of the quiet single-main rotor UAM concept studied in this work: "baseline" (Figure 3a) and "low-noise 30° blade droop" (Figure 3b). The complete vehicle consists of the rotor, hub, landing gear, tail, and fuselage. The physics of the NOTAR are not modeled in the CFD simulations, but they are included in the comprehensive analysis for correct vehicle trim.

If surface grids have sufficient overlap, the volume grids are then created using hyperbolic marching methods

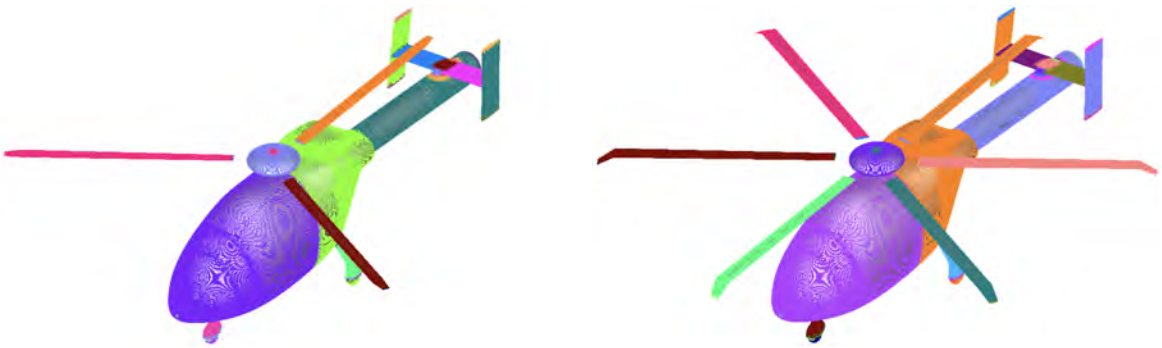

(a) Baseline geometry. **(b) Low-noise geometry, 30° blade droop.**

Fig. 3 QSMR overset surface grids for the complete vehicle, which includes the main rotor, main rotor hub, fuselage, tail, and landing gear. Figure 3a shows the vehicle with the baseline rotor geometry, with three blades and $R = 5.170\,\text{m}$. Figure3b shows the low-noise QSMR vehicle, with a six-bladed rotor, 30° droop, and $R = 5.378\,\text{m}$.

which extend the grid out to a fixed distance from the surface. Tight clustering in the normal direction near the wall is maintained to achieve good boundary layer resolution in viscous flow computations. The normal grid spacing of all grids at the walls maintains $y^+ \leq 1$. Mesh orthogonality is maximized to provide better solution accuracy. NB volume grids are extended ensuring that the outer boundaries are outside the boundary layer. The NB grids are contained inside the OB Cartesian grids, which extend to the far-field

Uniform spaced off-body Cartesian grids are utilized to resolve important flow features such as the wake region. Many Cartesian grids with successive levels of refinement based on proximity to the body are generated. Each Cartesian grid is twice as coarse as the previous level, and they expand the grid system to the far-field. The uniform spacing of the first OB grid layer, which contains the resolved wake region, is 10.0 % of the blade tip chord length c_{tip}. Cartesian grids extend to the far-field boundary, which is 20 radii away from the center of the vehicle in all directions.

B. Rotor Modeling

Two rotor modeling techniques have been used in this study: the mid-fidelity approach models the rotor as an infinitely thin disk whereas the high-fidelity approach resolves the rotor geometry. In the former case, the description of the blade geometry is replaced by a cylindrical polar grid containing the surface swept by the rotor. Using the *JKL* convention, the rotor plane lies on a constant J plane, with J increasing in the slipstream direction opposite to the thrust vector. K is the periodic direction that wraps around the polar axis with uniform azimuthal spacing. The L index increases along the blade span from the rotor root at $r < r_{\text{cutout}}$ to an outer boundary at $r > R$. The rotor is located between arbitrary L indices that depend on the cutout and tip positions. Grid resolution is clustered near the root and the tip, and in the slipstream direction, as shown in Figure 4a. The rotor disk grids with the complete vehicle are shown in Figure 4b.

The overset moving grids for the blades in the blade-resolved simulations are generated from the information in Table 1. It summarizes the rotor blade geometry properties for the baseline case ($V_{\text{tip}} = 700\,\text{ft/s}$) and the low-noise cases ($V_{\text{tip}} = 450\,\text{ft/s}$). With a lower tip speed for the low-noise configurations, the number of blades is increased from three to six to maintain the disk loading. Drooping the blade can further reduce the noise, by moving the tip vortices away from the following blade and hence reducing the blade-vortex interaction (BVI) noise. The blades use a modern, 11 % thick airfoil, with $\theta_{\text{tw}} = -12°$ twist and 60 % tapered tip (from $0.94R$). The root cutout is $0.15R$. The transition between the two different airfoil sections is smooth —linear interpolation with the radial stations. The blades from the low-noise configuration with droop have a tip droop of 30° applied at $r = 0.94R$.

The blade overset NB grids for the two cases are shown in detail in Figure 5. Surface grid resolution on the rotor blades is clustered in the chordwise direction near the airfoils leading and trailing edges, regions characterized by large pressure gradients. By the same token, the resolution is clustered near the blades' root and tip in the spanwise direction.

(a) Rotor disk overset grids.

(b) Rotor disk overset grids with the fuselage.

Fig. 4 Rotor disk overset grids for the QSMR UAM concept vehicle. The grids are clustered at the tip and root cutout, and extend axially from the disk placement.

Table 1 Summary of parameters related to the quiet single-main rotor helicopter baseline and low-noise configurations.

Parameter	Baseline	Low-noise
Number of blades/rotor	3	6
Radius R	5.170 m	5.378 m
Linear twist θ_{tw}	$-12.0°$	$-12.0°$
Root chord c_{root}	0.230 m	0.290 m
Tip chord c_{tip}	0.138 m	0.174 m
Thrust-weighted solidity σ	0.041	0.099
Design tip speed V_{tip}	700 ft/s	450 ft/s
WMTO	1663 kg	1841 kg

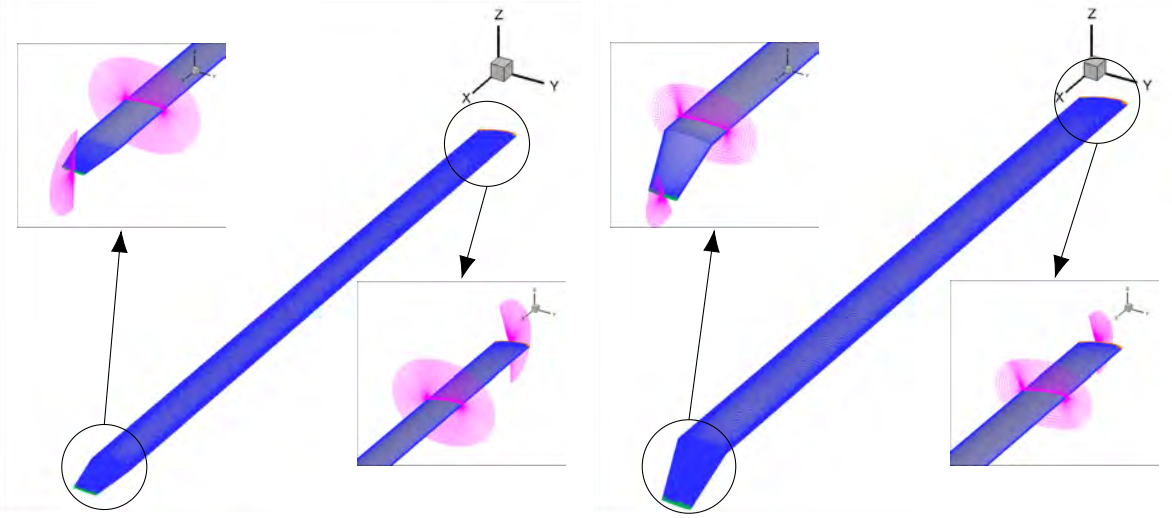

(a) Baseline geometry blade.

(b) Low-noise geometry blade, 30° blade droop.

Fig. 5 Blade overset grids for the quiet single-main rotor helicopter. O-grids are used for the main blade grid. For the tip and root, cap grids are used. Grid clustering near the leading edge, trailing edge, blade tip, and blade root is applied to solve the large pressure gradients near these regions.

C. High-Order Accurate Navier-Stokes Solver

The Navier-Stokes equations can be solved using finite differences with a variety of numerical algorithms and turbulence models. In OVERFLOW, the time-dependent Reynolds-Averaged Navier-Stokes (RANS) equations are solved in strong conservation form:

$$\frac{\partial \boldsymbol{q}}{\partial t} + \frac{\partial (\boldsymbol{F} - \boldsymbol{F}_\mathrm{v})}{\partial x} + \frac{\partial (\boldsymbol{G} - \boldsymbol{G}_\mathrm{v})}{\partial y} + \frac{\partial (\boldsymbol{H} - \boldsymbol{H}_\mathrm{v})}{\partial z} = \boldsymbol{0}, \tag{1}$$

with $\boldsymbol{q} = [\rho, \rho u, \rho v, \rho w, e]^\intercal$ the vector of conserved variables; $\boldsymbol{F}$, $\boldsymbol{G}$ and $\boldsymbol{H}$ the inviscid flux vectors; and $\boldsymbol{F}_\mathrm{v}$, $\boldsymbol{G}_\mathrm{v}$ and $\boldsymbol{H}_\mathrm{v}$ the viscous flux vectors.

For the rotor disk model, the RANS equations are solved with an HLLE++ upwind scheme, 5$^{\text{th}}$-order accurate spatial differencing, and scalar dissipation. The flow field around the blades is replaced by spatially- and time-averaged loads acting on the incoming flow. To that end, a source term [11] is added to the right-hand side of equation (1) for the cells where the rotor is located:

$$\boldsymbol{S} = \left[0, f_x, f_y, f_z, \boldsymbol{f} \cdot \boldsymbol{v}\right]^\intercal, \tag{2}$$

where $\boldsymbol{f}$ is the local force per unit area for the disk, able to vary with the radial and azimuthal positions. These aerodynamic forces are determined from airfoil measured characteristics stored as C81 formatted tables. The local angle of attack and Mach number for each blade section are updated at each time step of the simulation considering the most recently computed RANS solution.

For blade-resolved simulations, the diagonal central difference algorithm is used with the 5$^{\text{th}}$-order accurate spatial differencing option with scalar dissipation. The physical time step corresponds to 0.25° rotor rotation, together with up to 50 dual-time sub-iterations for 2.5 to 3.0 orders of magnitude drop in sub-iteration residual. The numerical approach and time step were previously validated for various rotor flows [17–19].

D. Hybrid Turbulence Modeling

The OVERFLOW code currently includes algebraic, one-equation, and two-equation turbulence models, including the choice of hybrid Reynolds-Averaged Navier-Stokes / Large Eddy Simulation (RANS/LES) models that close the RANS equations. In this study, the one equation Spalart-Allmaras [20] turbulence model is used primarily within the boundary layer.

The Detached Eddy Simulation (DES) [20] approach provides a good compromise between realism and computational cost. The intent of this model is to combine efficiently the best aspects of RANS and LES methodologies in a single solution. Near-wall regions are treated in RANS mode since turbulent scales can be very small and need to be modeled; and the rest of the flow is treated in LES mode, where the largest turbulent scales are grid-resolved. In this way, DES is a RANS/LES hybrid approach that mitigates the problem of artificially large eddy viscosity. The turbulence length scale d is replaced by $\bar{d}$:

$$\bar{d} = \min(d, C_\mathrm{DES} \Delta S), \tag{3}$$

which is the minimum of the distance from the wall d and C_DES times the local grid spacing ΔS.

The DES approach assumes that the wall-parallel grid spacing $\Delta S_{||}$ exceeds the thickness of the boundary layer δ so that the RANS model remains active near solid surfaces. If the wall-parallel grid spacing is smaller than the boundary layer thickness, $\Delta S_{||} < \delta$ then the DES Reynolds stresses can become under-resolved within the boundary layer; this may lead to non-physical results, including grid-induced separation. Using Delayed Detached Eddy Simulation (DDES) [21], the RANS mode is prolonged and is fully active within the boundary layer. The wall-parallel grid spacing used in this study does not violate the hybrid-LES validity condition; thus, DES and DDES should give similar results. Nevertheless, all computations have been performed using the DDES model for both NB and OB grids.

E. Comprehensive Analysis

Structural dynamics and rotor trim for the coupled calculations are performed using the comprehensive rotorcraft analysis code CAMRAD II [15]. CAMRAD II is an aeromechanics analysis of rotorcraft that incorporates a combination of advanced technologies, including multibody dynamics, nonlinear finite elements, and rotorcraft aerodynamics. The trim task finds the equilibrium solution for a steady-state operating condition, and produces the solution for performance, loads, and vibration. The aerodynamic model for the rotor blade is based on lifting-line theory, using two-dimensional airfoil characteristics and a vortex wake model. CAMRAD II has undergone extensive correlation with performance and loads measurements on rotorcraft.

F. Loose Coupling Overflow - CAMRAD II

A loose coupling approach between OVERFLOW and CAMRAD II based on a trimmed periodic rotor solution is utilized. The comprehensive code provides the trim solution and blade motions. The high-fidelity CFD calculates the airloads. That is, the CFD airloads replace the comprehensive airloads while using lifting line aerodynamics to trim and computational structural dynamics to account for blade deformations. For the actuator disk simulations, the motion interface is modified to account for the blade motions through control angles instead of quarter-chord displacement data. Figure 6 summarizes the loose coupling approach.

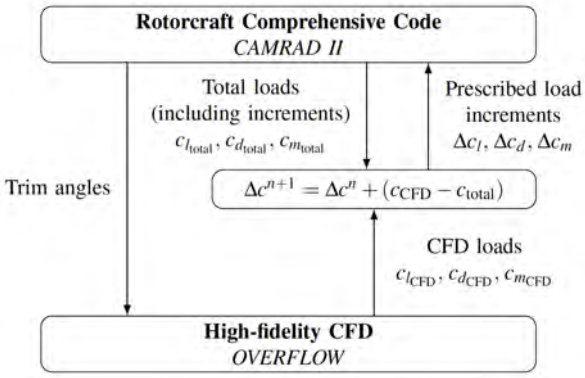

Fig. 6 Flow diagram for CFD/comprehensive analysis loose coupling methodology.

The simulation is initialized with a comprehensive analysis resulting in a trimmed rotor solution obtained with lifting line aerodynamics. This analysis creates initial quarter chord motions as a function of the radial position r and the azimuth ψ, for the rotor. In addition, the aircraft attitude is also obtained from CAMRAD II. The motions and aircraft pitch angle are given to the CFD. The CFD analysis accounts for the entire flow field, and therefore it only requires the structural motion. The CFD is run with the prescribed motions and angles, for two to three full rotor revolutions for the first coupling step. OVERFLOW outputs the normal force N' , pitching moment M' , and chord force C' as a function of radius and azimuth. Then, the aerodynamic force and moment coefficient increments Δc that are used in the comprehensive code at the next iteration $n + 1$ are calculated. The increments are the difference between the CFD loads and the comprehensive lifting line solution required to trim from the previous step n, plus the load increments from the previous step:

$$\Delta c^{n+1} = \Delta c^n + (c_{\text{CFD}} - c_{\text{total}}). \tag{4}$$

For the initial step, the increments are the difference between CFD and the total loads from the 0^{th} run in CAMRAD II:

$$\Delta c^1 = c_{\text{CFD}} - c_{\text{total}}. \tag{5}$$

The sectional pitching moment $M^2 c_m$, normal force $M^2 c_n$, and chord force $M^2 c_c$ coefficients are defined as:

$$M^2 c_m = \frac{M'}{1/2 \rho a^2 c}, \tag{6}$$

$$M^2 c_n = \frac{N'}{1/2 \rho a^2 c}, \tag{7}$$

$$M^2 c_c = \frac{C'}{1/2 \rho a^2 c}. \tag{8}$$

With the new quarter chord motions of the retrimmed rotor and the new aircraft attitude, the CFD is rerun. The previous CFD flow solution is used as a restart condition. The coupling is performed every 1/3, 2/3 or full revolution. The coupling solution is considered to be converged when collective and cyclic control angles and the CFD aerodynamic forces do not change between iterations. The CFD flow solution is usually converged after 10 to 20 rotor revolutions. The coupling procedure is valid as long as the rotor loads are periodic. This approach is still good if there is some aperiodicity in the vortex wake, which is often the case in high-resolution turbulent simulations.

For the disk model, the coupling is done every 1000 flow solution steps in OVERFLOW, which showed improved convergence over coupling every 2000 or 3000 steps. Convergence is achieved when collective and cyclic control angles and the CFD aerodynamic forces do not change between iterations within a small tolerance. There is no requirement for periodicity since the simulation is not time accurate.

III. Results

In the following paragraphs, the QSMR UAM concept vehicle simulations in hover with the OVERFLOW-CAMRAD II loose-coupling approach, using the rotor disk and the blade-resolved, will be presented. An initial mesh refinement study for the isolated rotor disk will be shown. Then, isolated rotor disk results will be analyzed for the three QSMR configurations (baseline, low-noise no droop, low-noise 30° droop). The next section will study the complete vehicle and the two approaches in OVERFLOW to simulate the rotor: the mid-fidelity rotor disk and the high-fidelity blade-resolved. To end the work, a tip losses model will be analyzed for the QSMR baseline geometry.

The flight conditions simulated are summarized in Table 2, which are representative of a UAM mission. Both low-noise without and with droop configurations are run using the same flight conditions.

Table 2 Flight conditions for the QSMR urban air taxi simulations.

Parameter	Baseline	Low-noise
h	5000 ft	5000 ft
T_∞	ISA +20°C	ISA +20°C
Ω	41.3 rad/s	25.5 rad/s
V_{tip}	213.36 m/s	137.16 m/s
M_{tip}	0.616	0.396
Re	1.6×10^6	1.3×10^6

A. Mesh Refinement Study

A mesh refinement study on the isolated disk of the QSMR vehicle has been carried out. The disk is simulated in hover, using the OVERFLOW-CAMRAD II coupling approach, and for the geometric parameters of the baseline QSMR vehicle case. Table 3 shows the details of the mesh refinement study. The objectives of this preliminary study are to assess and verify the gridding best practices for the rotor disk simulations in OVERFLOW. The "baseline" grid meets the minimum requirements for the actuator disk gridding criteria, with 10% c_{tip} for the minimum grid spacing. Following the JKL convention from OVERFLOW and CGT, the minimum grid spacing (ΔS_{min}) is applied at the root and tip locations (L_{root}, L_{tip}) spanwise, and at the disk location (J_{disk}) streamwise. The grid spacing of the OB L1 box corresponds to ΔS_{wake}, and is equal to the maximum grid spacing (ΔS_{max}) for the grids of the disk. A side view of the grids is presented in Figure 7, which shows a cut plane of the mesh of the rotor disk and OB grids. The simulations were run using the coupled OVERFLOW-CAMRAD II approach, with 600 Ivy Bridge CPUs on NASA's Supercomputer Pleiades. Wall-clock time ranged from 96 h for the extra fine case, to 10 h for the coarse case. The total number of grid points was 255 million grid points for the extra fine case and 8 million grid points for the coarse case.

The vortex wake geometry is visualized via Q-criterion iso-surfaces colored with the vorticity magnitude, as shown in Figure 8. A finer grid provides finer vortical structures and a more detailed flow solution. The rotor disk model is capable of reproducing flow features such as the contraction of the vortex wake as can be seen in the image. The disk plane is represented by using a translucid plane.

The performance of a hovering rotor is measured by the figure of merit, FM, which is defined as the ratio of ideal power to hover divided by the actual power required to hover. The figure of merit can be calculated as $\text{FM} = c_T^{3/2}/(\sqrt{2}c_Q)$. The figure of merit convergence history for the mesh refinement study is shown in Figure 9. The coupling cycle refers to the coupling step of the loosely-coupled approach. No trend is observed between the different cases on the figure of merit, and all appear to converge to similar values, ranging between FM = 0.727 and FM = 0.735, which represents only a 1% difference. In the remainder of this work, the "baseline" grid spacings have been applied, as they meet the minimum gridding spacing requirements of $\Delta S_{\text{min}} = 10\% c_{\text{tip}}$.

Table 3 Mesh refinement study on actuator disk for the QSMR baseline geometry.

Case	ΔS_{min}	ΔS_{max}	ΔS_{wake}	NB points	N total	Wall-clock time
Extra fine	5% c_{tip}	10% c_{tip}	10% c_{tip}	25.7 M	255.4 M	96 h
Fine	7.5% c_{tip}	20% c_{tip}	20% c_{tip}	8.0 M	100.5 M	49 h
Baseline	10% c_{tip}	30% c_{tip}	30% c_{tip}	2.2 M	34.8 M	19 h
Medium	15% c_{tip}	40% c_{tip}	40% c_{tip}	1.2 M	14.5 M	12 h
Coarse	20% c_{tip}	50% c_{tip}	50% c_{tip}	0.7 M	8.1 M	10 h

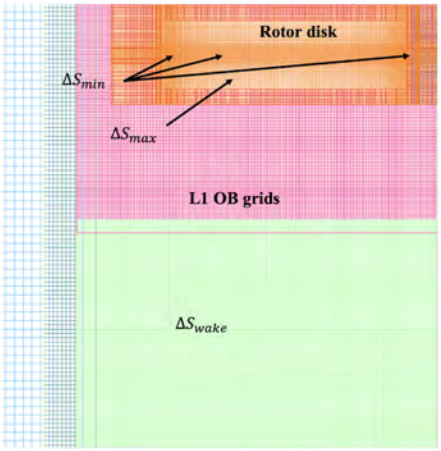

Fig. 7 Overset NB and OB grids for rotor disk simulations, isolated disk. Cut plane located at $y = 0$.

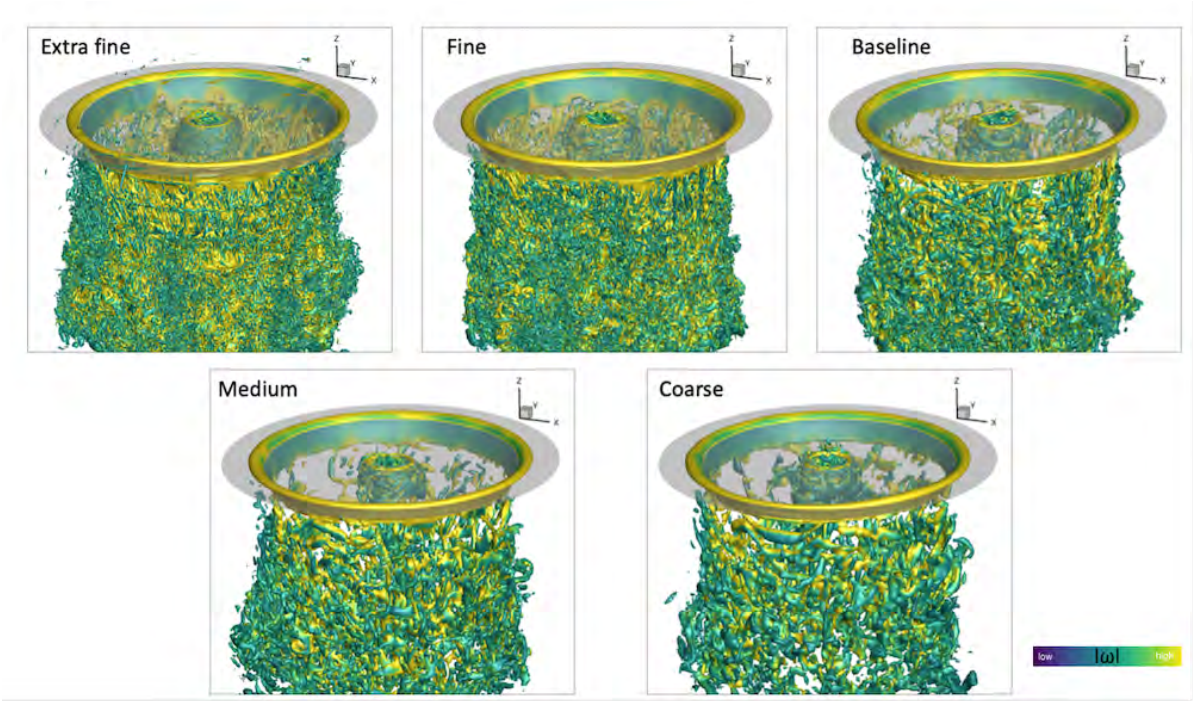

Fig. 8 Q-criterion vorticity iso-surfaces colored with vorticity magnitude for different grid refinements. The simulations have been run for the QSMR baseline geometry ($V_{\text{tip}} = 700$ ft/s) isolated rotor disk disk.

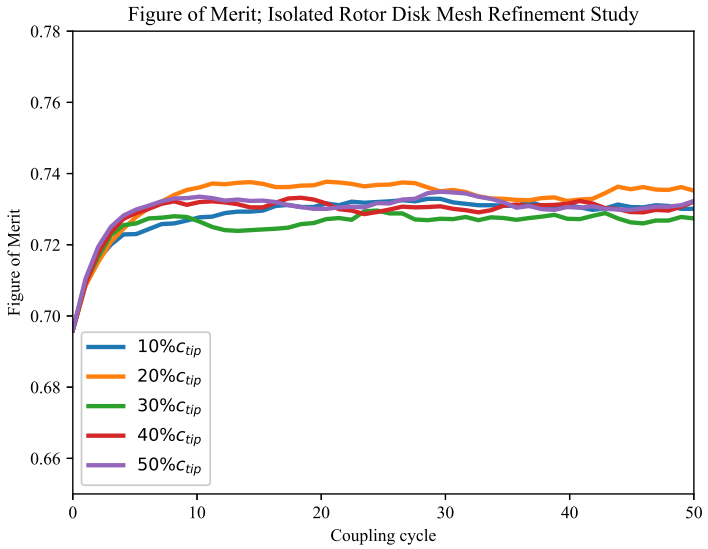

Fig. 9 Figure of Merit for the mesh refinement study.

B. Isolated Rotor Disk

In this section the results for the QSMR isolated rotor disk OVERFLOW-CAMRAD II simulations will be analyzed. The trim solution is considered converged when the comprehensive code airloads equal the CFD airloads, or when the control angles do not change with the iteration number. The simulations were run on NASA's supercomputers, using the gridding parameters from the previous section for the "baseline" mesh.

Figure 10 shows the trim angles for the three QSMR vehicle configurations studied. Good convergence is found after 15 to 20 coupling cycles. Generally, a longer runtime is required for the flow solution to allow the wake to develop and for the forces and moments on other components in the wake to reach convergence. The flapping angles β_{1s} and β_{1c}. and the collective angle θ_0 are similar for the low-noise configurations, with the main difference in values for the coning angle β_0, giving a lower value for the drooped configuration. Low-noise configurations trim to a higher collective angle than the baseline configuration.

Figure 11 displays the sectional normal force coefficient distributions for the QSMR isolated disk in hover. The positive direction of the azimuth angle ψ is counter-clockwise (CCW), which corresponds to the direction of rotation. The coefficient is non-dimensionalized by the speed of sound. The normal force coefficient increases towards the tip ($r/R = 1$). The distributions are almost axi-symmetric, as it should be expected for the isolated rotor disk in hover. Higher values of $M^2 c_n$ are found for the baseline QSMR isolated disk simulations.

The thrust coefficient, torque coefficient, and figure of merit for the three QSMR configurations are shown in Table 4. Trimmed thrust and torque coefficients converge to higher values for the low-noise configurations as the QSMR vehicle is heavier (see WMTO, Table 1). Same thrust for both low-noise QSMR vehicles is obtained, as expected. The torque is slightly lower for the drooped blade, thus giving higher performance as seen by the figure of merit. High-solidity and lower tip speeds give a better hovering rotor performance as predicted by the rotor disk approach.

Table 4 Thrust and torque coefficients for the isolated rotor disk in hover.

	Baseline	**Low-noise 0° droop**	**Low-noise 30° droop**
Thrust coefficient c_T	0.00433	0.01071	0.01071
Torque coefficient c_Q	0.000277	0.001002	0.000989
Figure of merit FM	0.727	0.782	0.793

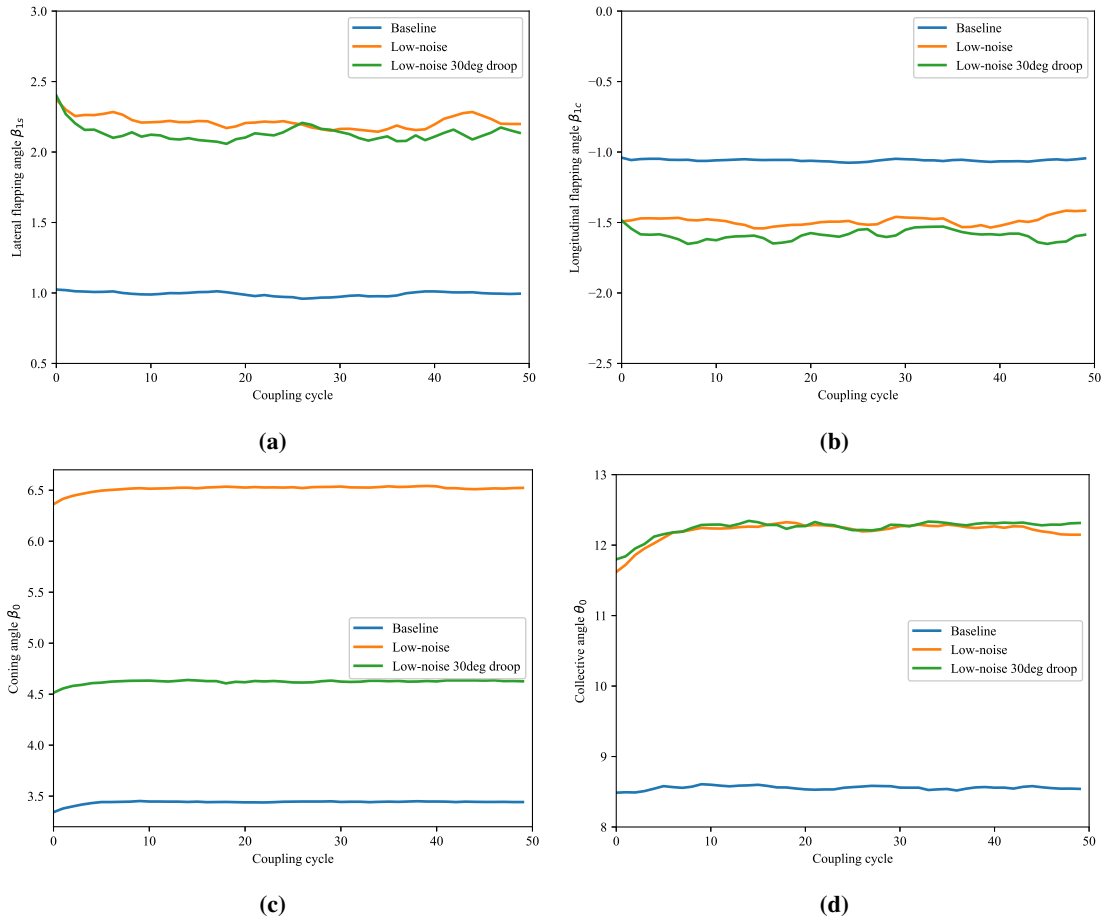

Fig. 10 Convergence history of the rotor trim angles in hover for the QSMR isolated rotor disk: (a) longitudinal flapping angle β_{1s}, (b) lateral flapping angle β_{1c}, (c) coning angle β_0, and (d) collective angle θ_0.

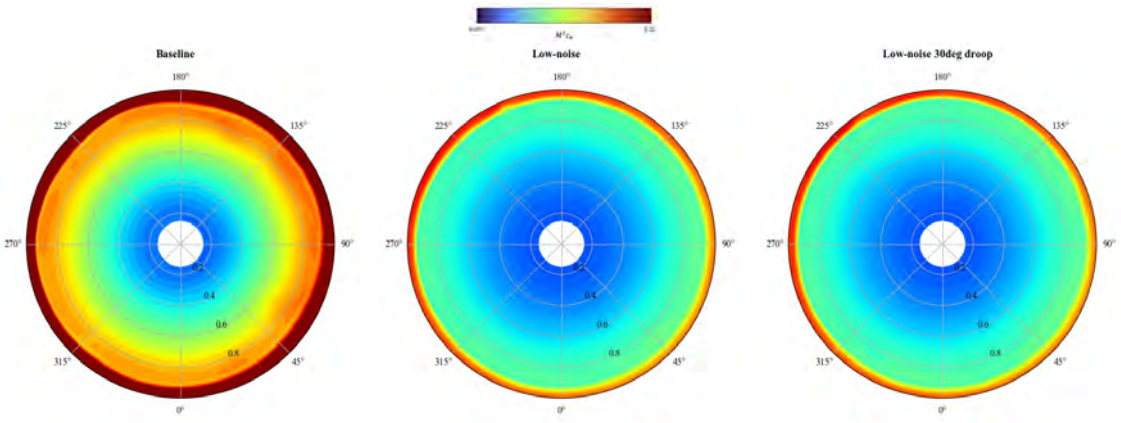

Fig. 11 Sectional normal force coefficient M^2c_n distribution for the QSMR isolated rotor disk: (a) baseline QSMR vehicle, (b) low-noise 0° droop QSMR vehicle, and (c) low-noise 30° droop QSMR vehicle.

C. QSMR Complete Vehicle

In this section the complete vehicle is analyzed in hover. The mid-fidelity rotor disk solution is compared to the high-fidelity unsteady blade-resolved solution [4]. In the absence of experimental data, the high-fidelity flow solution is considered as reference values.

Table 5 presents the number of grid points and the time it took to obtain the solution for both approaches. Rotor disk simulations were run using 1000 processors and took less than 48 h to complete. The unsteady blade-resolved simulations had to be run with 2000 to 2200 processors and run for 240 h (10 days). The difference of computer power necessary to run the two different approaches is significant, and while the rotor disk approach is of lower fidelity, it can prove very useful when many simulations need to be run. The computer time is reduced by more than 85%.

Figure 12 shows the convergence history for the control angles for the rotor disk and blade-resolved simulations. Trim angles converge after 10 to 20 coupling cycles. Similar values for the flapping and coning angles are obtained when comparing the rotor disk and the blade-resolved results. Small differences can be observed with the previous results for the isolated disk. Adding the fuselage to the simulations changes the trim solution, and the disk performance is affected by the rotor-airframe aerodynamic interactions. The collective angle is relatively higher for the low-noise configurations compared to the baseline geometry when using the rotor disk approach. In addition, the blade-resolved simulation predicts a higher collective angle for the low-noise without blade tip droop, which will affect the performance parameters.

The wake geometry for the different cases is shown in Figures 13 to 16, for the high- and mid-fidelity simulations. Q-criterion vorticity iso-surfaces colored with the vorticity magnitude are shown in Figure 13 for the high-fidelity simulations. Vortex wake breakdown happens after 2 to 4 revolutions. The magnitude of vorticity on the vortices is similar between the baseline and low-noise no-droop configurations (Figures 13a, 13b). The tip droop changes the position of the primary tip vortex and decreases its strength, as seen by the lower vorticity magnitude (Figure 13c). In addition, a secondary weak vortex is formed where the droop starts, due to the change in aerodynamic distribution at that section of the blade. A closer view of these phenomena is presented in Figure 14. In the images, it can be observed in detail BVI in hover for the three cases, with the drooped rotor having secondary vortices (Figure 14c). The high-fidelity solution portrays an accurate and detailed description of the flow field.

The vortex wake for the mid-fidelity OVERFLOW simulations is shown in Figure 15. The mid-fidelity simulation obtains a time- and space-averaged rotor solution. Since the loading is distributed across the entire rotor disk, vorticity is concentrated in a vortex sheet at the tip, which outlines the edge of the modeled rotor.

A comparison of the vorticity contours at a $y = 0$ plane between the high- and mid-fidelity solutions is presented in Figure 16. These images provide valuable insights into the generation of vorticity. In the blade-resolved case, boundary layers that contain vorticity formed in the upper and lower surfaces of the blade form wake shear layers upon leaving the trailing edge. For the rotor disk case, vorticity is generated in the form of vortex sheets at the edges of the disk and transported downstream with the flow. The vorticity magnitude is greater in the vortex cores of the high-fidelity solution than in the tip vortex sheets of the mid-fidelity solution.

The thrust coefficient, torque coefficient, and figure of merit for the three QSMR configurations are shown in Tables 6 and 7 for the blade-resolved and rotor disk simulations, respectively. Thrust coefficient trims to the same values independently of the approach to simulate the rotor flow. The differences are observed for the torque coefficient. In the case of the baseline geometry, the torque predicted is 2% lower when using the rotor disk. The figure of merit obtained with the rotor disk approach is 2% higher when compared to the blade-resolved simulations. When comparing with the isolated disk (Table 4), the performance in terms of the FM is 3% for the complete vehicle using rotor disk, as the fuselage acts as a ground effect on the rotor increasing its performance. Rotor-airframe aerodynamic interactions are captured with the rotor disk approach too. When analyzing the low-noise configurations, the high-fidelity simulations predict that drooping the blade increases the power required to hover, and the FM of the low-noise with 30° droop QSMR geometry is 3% lower compared to the rotor geometry without droop. The mid-fidelity simulations do not capture the details of the flow such as BVI or the secondary tip vortices from the drooped blade, predicting slightly higher performance in terms of the FM of 2%. Between the mid-fidelity and the high-fidelity simulations for the low-noise configurations, the rotor disk overpredicts the FM for the drooped blade by 3% and underpredicts the FM for the blade without droop by 2%.

The history convergence for the figure of merit is presented in Figure 17. Although the rotor disk model fails to predict the lower performance of the drooped blade QSMR geometry, differences with the high-fidelity approach in terms of performance are of 3% or lower. The rotor disk model can be an alternative to the computationally expensive high-fidelity CFD simulations of single rotor configurations such as the QSMR. However, performance prediction using the rotor disk approach worsens in multi-rotor configurations, like it has been observed for the tilt-wing vehicle as

shown in [12]. The complex interactional aerodynamics of multi-rotor vehicles are challenging to model and recreate with simplified approaches. High-fidelity CFD continues to be the right tool to simulate and analyze these type of configurations.

Table 5 Number of grid points, processors used, and wall-clock time for the rotor disk and blade-resolved simulations, for the QSMR complete vehicle.

Parameter	Rotor Disk	Blade-Resolved
Number of points	≈ 65 M	≈ 500 M
Number of processors	1000	2000 to 2200
Wall-clock time	32 h	240 h

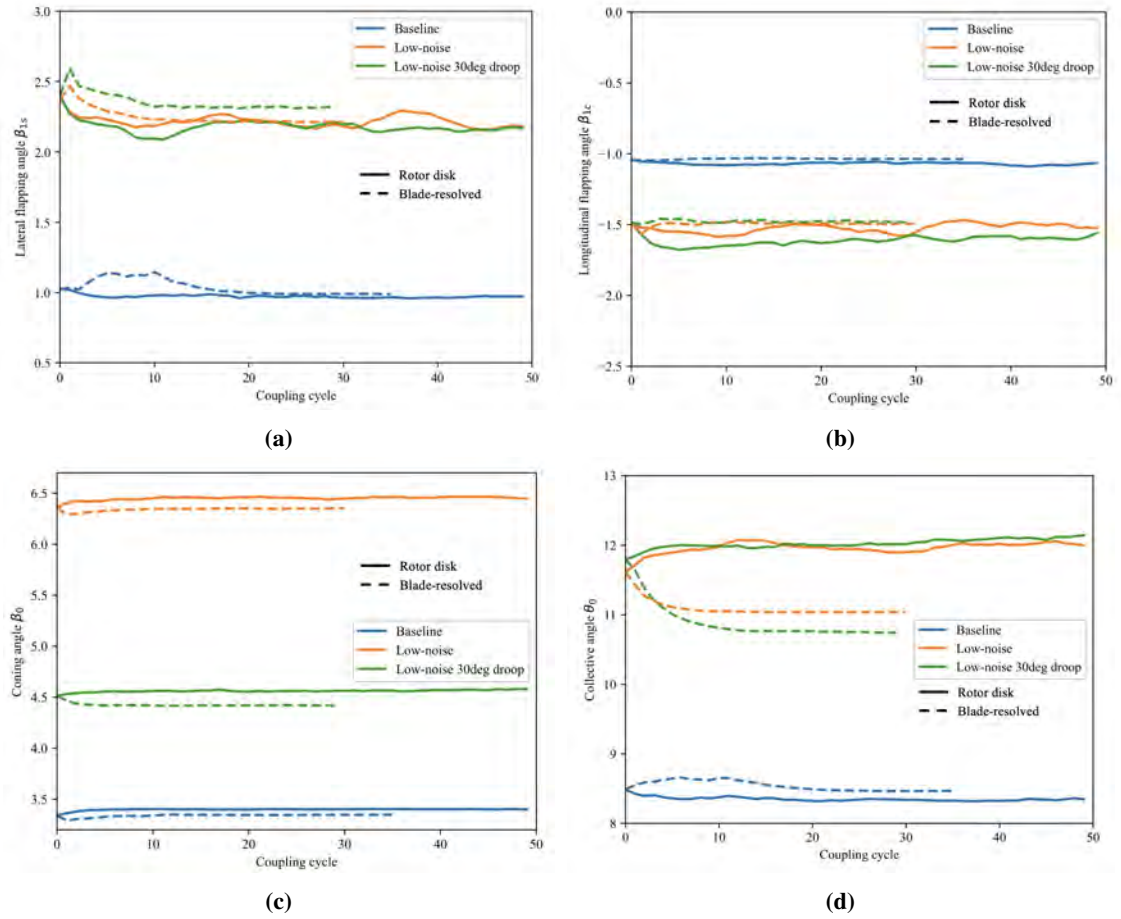

Fig. 12 Convergence history of the rotor trim angles in hover for the QSMR complete vehicle, with the rotor disk (mid-fidelity) and the blade-resolved (high-fidelity): (a) longitudinal flapping angle β_{1s}, (b) lateral flapping angle β_{1c}, (c) coning angle β_0, and (d) collective angle θ_0.

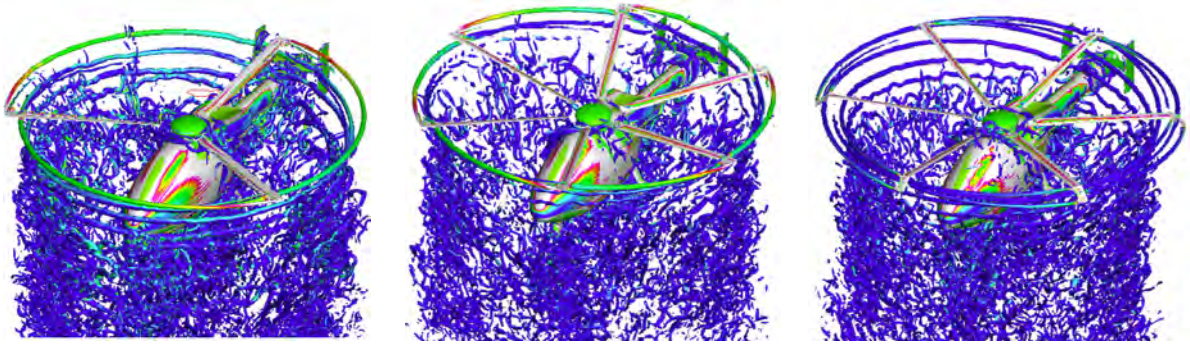

(a) Baseline geometry. (b) Low-noise geometry no blade droop. (c) Low-noise geometry 30° blade droop.

Fig. 13 QSMR wake geometry obtained from unsteady blade-resolved OVERFLOW in hover. Q-criterion vorticity iso-surfaces colored with the vorticity magnitude, oblique view.

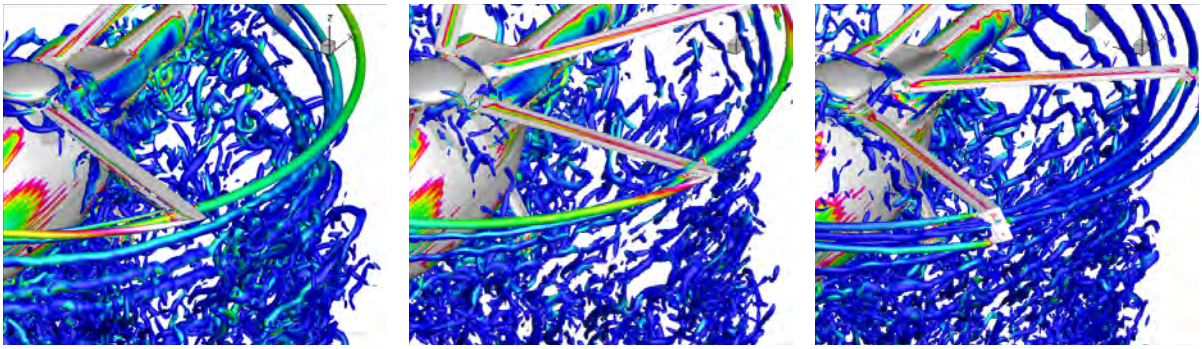

(a) Baseline geometry. (b) Low-noise geometry no blade droop. (c) Low-noise geometry 30° blade droop.

Fig. 14 QSMR wake geometry obtained from unsteady blade-resolved OVERFLOW in hover. Q-criterion vorticity iso-surfaces colored with the vorticity magnitude. Close-up view to show the blade tip vortices.

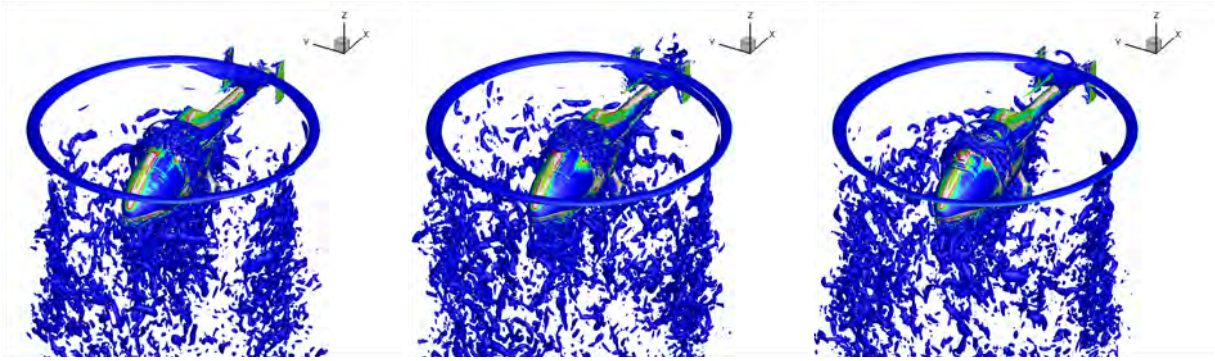

(a) Baseline geometry. (b) Low-noise geometry no blade droop. (c) Low-noise geometry 30° blade droop.

Fig. 15 QSMR wake geometry obtained from rotor disk OVERFLOW in hover. Q-criterion vorticity iso-surfaces colored with the vorticity magnitude, oblique view.

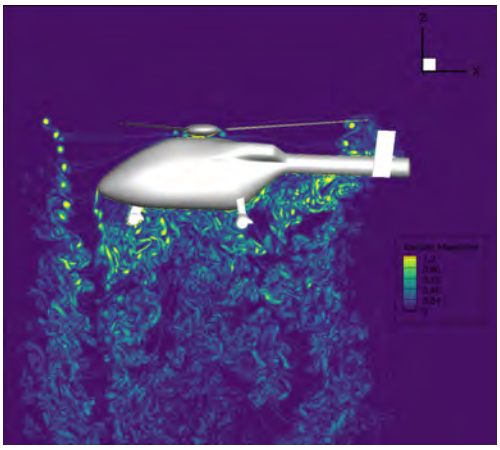

(a) Blade-resolved QSMR baseline geometry.

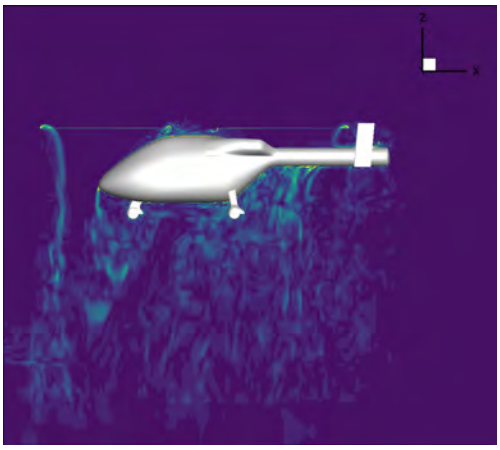

(b) Rotor disk QSMR baseline geometry.

Fig. 16 Vortex wake for the baseline QSMR geometry. Vorticity contours, side view.

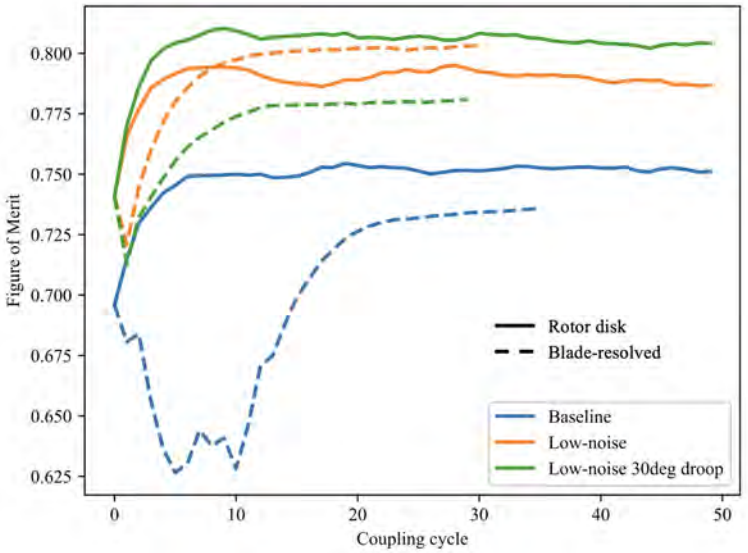

Fig. 17 Figure of Merit for the complete vehicle QSMR simulations.

Table 6 Thrust and torque coefficients for the complete vehicle using blade-resolved (high-fidelity) in hover.

	Baseline	**Low-noise 0° droop**	**Low-noise 30° droop**
Thrust coefficient c_T	0.00433	0.01071	0.01071
Torque coefficient c_Q	0.000274	0.000976	0.001004
Figure of merit FM	0.736	0.803	0.782

Table 7 Thrust and torque coefficients for the complete vehicle using rotor disk (mid-fidelity) in hover.

	Baseline	**Low-noise 0° droop**	**Low-noise 30° droop**
Thrust coefficient c_T	0.00433	0.01071	0.01071
Torque coefficient c_Q	0.000268	0.000996	0.000975
Figure of merit FM	0.751	0.787	0.804

D. Tip Loss Model

Similar to aircraft wings, trailed vortex inflow over the tip of a rotor blade reduces its lifting capability. The rotor disk model uses two-dimensional airfoil data and is not capable of taking this effect into account. Prandtl's tip loss model, described in [22], consists in applying an effective blade radius, usually at 98% of the blade radius. The effective blade radius is unaffected by the tip loss. The remaining percentage of the blade sees a loss in lift, with zero lift applied at the tip. To investigate the effect of the tip loss model in this work, Prandtl's tip loss model is utilized for the complete vehicle baseline QSMR geometry. The results are presented in Figure 18.

Figure 18a shows a comparison of the normal force distribution per unit span. The effect of applying the tip loss model on the rotor disk changes the normal force distribution, to a similar distribution to that obtained with the high-fidelity simulations, recreating the loss in lift at the tip. In addition, it can be observed the level of details the blade-resolved simulations can capture: the small dip reflects the change in blade loading due to BVI. Without a tip loss model, the normal force coefficient increases all the way to the tip.

Figure 18b displays the convergence history for the figure of merit for the complete vehicle QSMR baseline geometry simulations. The rotor disk without tip losses overpredicts the FM by 2% when comparing to the high-fidelity simulations. Introducing the tip loss model corrects the loading prediction at the tip, and the final FM predicted is FM = 0.735. This value is much closer to the one calculated with the blade-resolved simulations, with a difference lower than 0.2%.

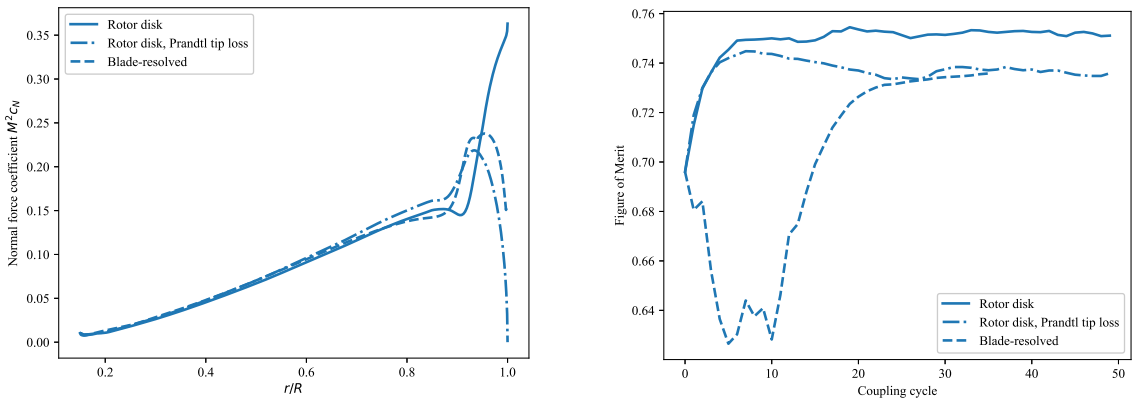

(a) Normal force coefficient M^2c_n radial distribution. **(b) Figure of Merit convergence history.**

Fig. 18 Tip loss model applied to the rotor disk simulations for the complete vehicle QSMR baseline geometry in hover.

IV. Summary

A multi-fidelity study of NASA's QSMR UAM vehicle concept in hover has been performed. High- and mid-fidelity CFD simulations using OVERFLOW have been loosely coupled to the rotorcraft comprehensive code CAMRAD II for accurate calculations. The high-fidelity, time-accurate approach individually tracks and resolves each blade using body-fitted rotating grids. The mid-fidelity approach represents the rotor as an infinitely thin disk and uses source terms in the Navier-Stokes equations to simulate its effect on the airflow.

An initial mesh refinement study was performed. Five different meshes were simulated for an isolated rotor disk. With a coarser grid, less details were captured in the vortex wake. The loosely-coupled approach trimmed to similar conditions, with differences on the figure of merit of less than 1% for all cases. The baseline mesh was chosen for the rest of the work to satisfy the meshing requirements for the rotor disk model in OVERFLOW.

The isolated rotor disk was then analyzed for the three different QSMR geometries. Changing the rotor design affected the aerodynamic distributions on the disk and the overall performance. The low-noise configurations have a higher figure of merit than the baseline QSMR geometry.

Next, the complete vehicle was simulated using the rotor disk and the blade-resolved approaches in OVERFLOW. A comparison of the trim solution, wake geometry, and rotor performance was presented. Effects such as BVI or secondary vortices observed with the high-fidelity CFD simulations could not be reproduced by the disk model. Satisfactory agreement was obtained in terms of the figure of merit, with differences lower than 3%.

A tip loss model was analyzed with the objectives to improve the modeling of the rotor disk. Indeed, the figure of merit prediction error was further decreased to less than 0.2%.

The rotor disk model shows to be an effective alternative to circumvent the complexity and large computational requirements associated with simulating unsteady flows of rotating blades. The cost of turnaround time was reduced by more than 85%. This is particularly interesting for optimization applications or as an initial design tool, where this approach can be used as a surrogate model of the physical moving blades.

Acknowledgments

This work is supported by the Revolutionary Vertical Lift Technology (RVLT) project (PM: Susan Gorton; TL: Brian Allan). The computations utilized the Pleiades, Electra, and Aitken supercomputers at the NASA Advanced Supercomputing Division. The authors would like to thank Wayne Johnson, Pieter Buning, Jasim Ahmad, Chris Silva, Gloria Yamauchi, and Brian Allan for helpful discussions.

References

[1] Johnson, W., Silva, C., and Solis, E., "Concept Vehicles for VTOL Air Taxi Operations", The AHS International Technical Meeting on Aeromechanics Design for the Transformative Flight, San Francisco, California, January 2018.

[2] Johnson, W. and Silva, C., "NASA concept vehicles and the engineering of advanced air mobility aircraft", The Aeronautical Journal 2022, 126, pp. 59-91. https://doi.org/10.1017/aer.2021.92

[3] Johnson, W., "A Quiet Helicopter for Air Taxi Operations", VFS Aeromechanics for Advanced Vertical Flight Technical Meeting, San Jose, CA, January 21–23, 2020.

[4] Ventura Diaz, P., Garcia Perez, D., and Yoon, S., "Computational Analysis of a Quiet Single-Main Rotor Helicopter for Air Taxi Operations", Vertical Flight Society 78th Annual Forum, Dallas, Texas, May 2022.

[5] Garcia Perez, D., Ventura Diaz, P., and Yoon, S., "High-Fidelity Simulations of a Tiltwing Vehicle for Urban Air Mobility", AIAA Paper 2023-2282, The AIAA SciTech Forum 2023, January 2023. https://doi.org/10.2514/6.2023-2282

[6] Ventura Diaz, P., and Yoon, S.,"High-Fidelity Simulations of a Quadrotor Vehicle for Urban Air Mobility", AIAA Paper 2022-0152, The AIAA SciTech Forum 2022, January 2022. https://doi.org/10.2514/6.2022-0152

[7] Ventura Diaz, P., Johnson, W., Ahmad, J., and Yoon, S., "Computational Study of the Side-by-side Urban Air Taxi Concept", VFS 75th Annual Forum, Philadelphia, Pennsylvania, May 2019.

[8] Ventura Diaz, P. and Yoon, S., "High-Fidelity Computational Aerodynamics of Multi-Rotor Unmanned Aerial Vehicles", AIAA Paper 2018-1266, The AIAA SciTech Forum 2018, Kissimmee, Florida, January 2018. https://doi.org/10.2514/6.2018-1266

[9] Spalart, P., "On the simple actuator disk", Journal of Fluid Mechanics, 494, 399-405, 2003. https://doi.org/10.1017/S0022112003006128

[10] Chaffin, M. S., and Berry J. D, "Helicopter Fuselage Aerodynamics Under a Rotor by Navier-Stokes Simulation", in American Helicopter Society 51st Annual Forum, Fort Worth, TX, May 1997.

[11] Ahmad, J. U., "Application of Rotor Disk Model in the OVERFLOW CFD Code", NASA, Tech. Rep. NASA/TM-2022-0005496, April 2022.

[12] Garcia Perez, D., Ventura Diaz, P., and Yoon, S., "A Comparison of Rotor Disk Modeling and Blade-Resolved CFD Simulations for NASA's Tiltwing Air Taxi", VFS 79th Annual Forum, West Palm Beach, Florida, May 2023.

[13] Pulliam, T. H., "High Order Accurate Finite-Difference Methods: as seen in OVERFLOW", AIAA Paper 2011-3851, 20th AIAA Computational Fluid Dynamics Conference, Honolulu, Hawaii , June 2011. https://doi.org/10.2514/6.2011-3851

[14] Chan, W. M., Gomez, R. J., Rogers, S. E., Buning, P. G., "Best Practices in Overset Grid Generation", AIAA Paper 2002-3191, The 32nd AIAA Fluid Dynamics Conference, St. Louis, Missouri, June 2002. https://doi.org/10.2514/6.2002-3191

[15] Johnson, W., "Rotorcraft Aerodynamic Models for a Comprehensive Analysis", American Helicopter Society 54th Annual Forum, Washington, D. C., May 1998.

[16] Haimes, R., and Dannenhoffer, J. F., "The Engineering Sketch Pad: A Solid-Modeling, Feature-Based, Web-Enabled System for Building Parametric Geometry", AIAA Paper 2013-3073, The 21st AIAA Computational Fluid Dynamics Conference, San Diego, California, June 2013. https://doi.org/10.2514/6.2013-3073

[17] Yoon, S., Chaderjian, N. M., Pulliam, T. H., and Holst, T. L., "Effect of Turbulence Modeling on Hovering Rotor Flows", AIAA Paper 2015-2766, The 45th AIAA Fluid Dynamics Conference, Dallas, Texas, June 2015. https://doi.org/10.2514/6.2015-2766

[18] Yoon, S., Lee, H. C., and Pulliam, T. H., "Computational Analysis of Multi-Rotor Flows", AIAA Paper 2016-0812, The 54th AIAA Aerospace Sciences Meeting, AIAA SciTech Forum, San Diego, California, January 2016. https://doi.org/10.2514/6.2016-0812

[19] Yoon, S. Lee, H. C., and Pulliam, T. H., "Computational Study of Flow Interactions in Coaxial Rotors", The AHS Technical Meeting on Aeromechanics Design for Vertical Lift, San Francisco, California, January 2016.

[20] Spalart, P. R., Jou, W-H., Strelets, M., and Allmaras, S. R., "Comments on the Feasibility of LES for Wings and on a Hybrid RANS/LES Approach", Advances in DNS/LES, Greyden Press, 1997, pp. 137-147.

[21] Spalart, P. R., "Strategies for Turbulence Modeling and Simulations", International Journal of Heat and Fluid Flow, 21, 2000, pp. 252-263.

[22] Leishman, J. G., "Helicopter Aerodynamics", 2nd ed. Maryland: Cambridge University Press, 2006.